

Two-dimensional electron systems in ATiO_3 perovskites (A = Ca, Ba, Sr): control of orbital hybridization and order

T. C. Rödel,^{1,2,*} M. Vivek,³ F. Fortuna,¹ P. Le Fèvre,² F. Bertran,²
R. Weht,^{4,5} J. Goniakowski,⁶ M. Gabay,³ and A. F. Santander-Syro^{1,†}

¹*CSNSM, Univ. Paris-Sud, CNRS/IN2P3, Université Paris-Saclay, 91405 Orsay Cedex, France*

²*Synchrotron SOLEIL, L'Orme des Merisiers, Saint-Aubin-BP48, 91192 Gif-sur-Yvette, France*

³*Laboratoire de Physique des Solides, CNRS, Univ. Paris-Sud,*

Université Paris-Saclay, 91405 Orsay Cedex, France

⁴*Gerencia de Investigación y Aplicaciones, Comisión Nacional de Energía Atómica,
Avenida General Paz y Constituyentes, 1650 San Martín, Argentina*

⁵*Consejo Nacional de Investigaciones Científicas y Técnicas (CONICET), Buenos Aires, Argentina*

⁶*Institut des Nanosciences de Paris, UMR 7588,*

CNRS and Université Paris-6, 4 place Jussieu, 75252 Paris cedex 05, France

We report the existence of a two-dimensional electron system (2DES) at the (001) surface of CaTiO_3 . Using angle-resolved photoemission spectroscopy, we find a hybridization between the d_{xz} and d_{yz} orbitals, not observed in the 2DESs at the surfaces of other ATiO_3 perovskites, *e.g.* SrTiO_3 or BaTiO_3 . Based on a comparison of the 2DES properties in these three materials, we show how the electronic structure of the 2DES (bandwidth, orbital order and electron density) is coupled to different typical lattice distortions in perovskites. The orbital hybridization in orthorhombic CaTiO_3 results from the rotation of the oxygen octahedra, which can also occur at the interface of oxide heterostructures to compensate strain. More generally, the control of the orbital order in 2DES by choosing different A-site cations in perovskites offers a new gateway towards 2DESs in oxide heterostructures beyond SrTiO_3 .

Introduction.- ABO_3 perovskites, where B is a transition-metal (TM) ion, present many appealing phenomena, including ferroelectricity, ferromagnetism, superconductivity and strong electron-correlations [1, 2]. One reason for such a diversity is that the perovskite lattice can accommodate a large variety of differently sized A and B cations as described by Goldschmidt's tolerance factor [3]. This factor can be widely varied by the size of the A-site cation, resulting in different lattice distortions which strongly influence the electronic structure [4, 5].

Such a variety of functionalities within the same oxide family, together with the epitaxial compatibility amongst many of its members, has boosted the interest in oxide heterostructures over the last two decades. One prime example of these emerging properties is the two-dimensional electron system (2DES) found at the $\text{LaAlO}_3/\text{SrTiO}_3$ interface [6], which shows a wide range of properties including the coexistence of superconductivity and magnetism [7, 8] as well as a possibly unusual electron pairing mechanism [9]. More recently, the discoveries of 2DESs at bare surfaces of various perovskites such as the paraelectric SrTiO_3 [10–14], the strong spin-orbit coupled KTaO_3 [15–17], the catalyst TiO_2 anatase [18], or the ferroelectric BaTiO_3 [19] triggered new avenues of research by providing deep insight into the microscopic electronic structure of such 2DESs, including orbital order, symmetries, and electron-phonon interaction effects [10, 11, 20, 21].

Here we report the discovery of a 2DES at the (001) surface of CaTiO_3 . Moreover we find a significant hybridization between the d_{xz} and d_{yz} orbitals forming the

2DES, not observed in the 2DES's at the surface of other perovskite titanates, and show that it is induced by the rotation of the oxygen octahedra in the orthorhombic lattice resulting from the small size of the Ca ion. This is very appealing, as the possibility to use octahedral tilts to control the properties of oxide interfaces, such as magnetism, has attracted much attention lately [22–24]. To further explore the connection between lattice distortions in the perovskites and electronic structures in 2DES, we compare the 2DESs measured by ARPES at the surface of different titanates, ATiO_3 (A = Ca, Ba, Sr) [19]. We thus show that the orbital order, orbital symmetries (hybridization between different orbital characters) and bandwidths all depend on the size of the A-site cation.

Methods.- The ARPES measurements were conducted at the Synchrotron Radiation Center (SRC, University of Wisconsin, Madison) and the CASSIOPEE beamline of Synchrotron Soleil (France) at temperatures $T = 7 - 20$ K and pressures lower than $P = 6 \times 10^{-11}$ Torr. Details on the surface preparation and creation of the 2DES are discussed in the [Supplementary Material](#). Density Functional Theory (DFT) calculations were carried out on bulk CaTiO_3 . Values of the lattice parameters, tilt angles and band gaps were estimated and compared to experimental data reported in [25]. Of the three exchange-correlation functionals tested, the hybrid one (HSE06) gave the best agreement with the experimental values (see [Supplementary Material](#) for a comparison of the results obtained with different functionals). With this choice, the calculated lattice parameters differ from the experimental estimates by less

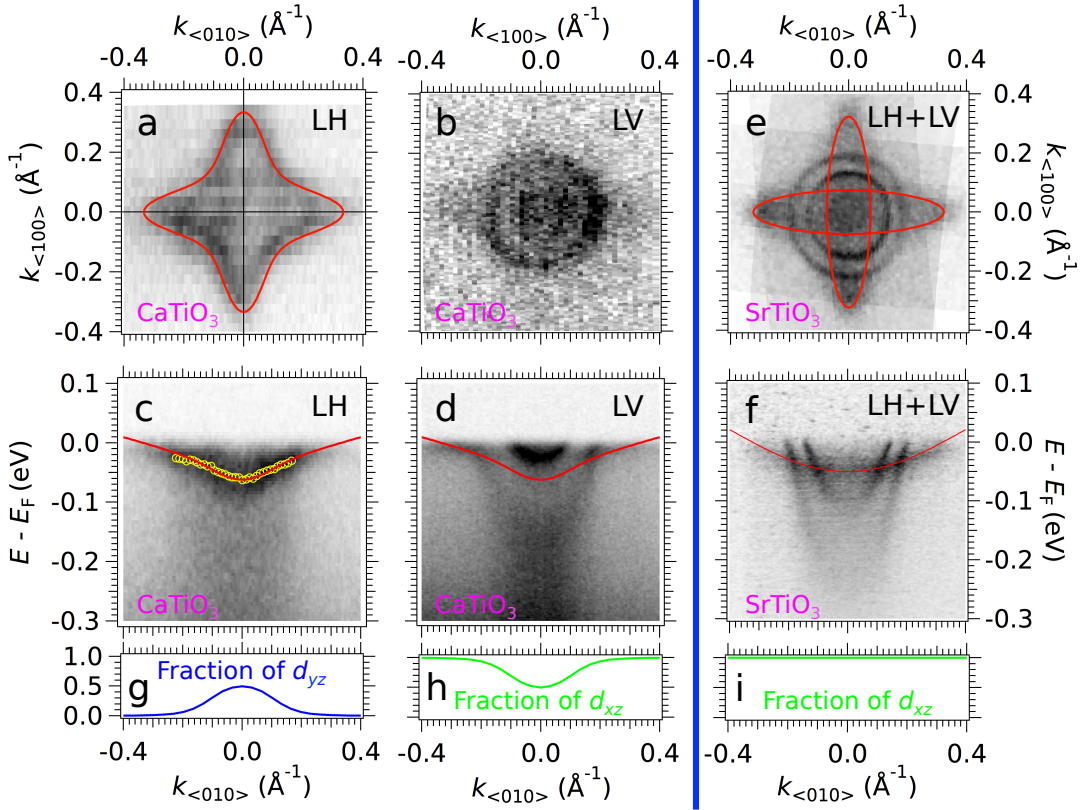


FIG. 1. (a, b) Fermi surface intensity maps of the 2DES measured at the surface of $\text{CaTiO}_3(001)$ close to Γ_{005} ($h\nu = 57$ eV) using linear horizontal (LH) polarization, and close to Γ_{115} ($h\nu = 67$ eV) using linear vertical (LV) polarization, respectively. (c, d) $E - k$ intensity maps measured at Γ_{005} using LH and LV polarization. The red curves are based on a one-layer tight-binding model assuming orbital hybridization between the d_{xz} and d_{yz} orbitals. The yellow markers in (c) are the peak positions of the fits of the energy distribution curves. (e, f) Fermi surface and $E - k$ map corresponding to the electronic structure of the 2DES at the (001) surface of SrTiO_3 . The shown intensity maps are a superposition of measurements using LH polarization at $h\nu = 90$ eV and LV polarization at $h\nu = 47$ eV. The red curves are, in this case, based on a tight-binding model *without* hybridization between the different t_{2g} orbitals. (g, h, i) Momentum-resolved fraction of orbital character of the d_{xz} or d_{yz} band visible in the $E - k$ maps in (c, d, f) based on the tight-binding model showing the orbital hybridization in the 2DES at the (001) surface of CaTiO_3 .

than 0.01 \AA and the tilt angles by less than 0.2° . The band gap is estimated to be 3.62 eV as compared to the experimental value of 3.50 eV [26]. All through this paper, directions and planes are defined in the quasi-cubic cell of CaTiO_3 . In this way, the (x, y, z) axes used to express orbitals and wave functions are defined along the Ti-Ti directions. In contrast, for experimental convenience, the indices h, k and l of Γ_{hkl} correspond to the reciprocal lattice vectors of the orthorhombic unit cell.

Experimental results.- Figs. 1(a, b) show the different observed Fermi surfaces in the (001) plane of pseudo-cubic CaTiO_3 . They were measured, respectively, around Γ_{005} using $h\nu = 57$ eV photons with linear vertical (LV) polarization, and around Γ_{115} using $h\nu = 67$ eV photons with linear horizontal (LH) polarization. One Fermi sheet consists of a four-pointed star as shown in Fig. 1(a), while two other Fermi sheets are circular as seen in

Fig. 1(b). Figs. 1(c, d) present the energy-momentum maps close to the bulk Γ_{005} point along the $\langle 010 \rangle$ direction, using respectively LH and LV polarizations. In Fig. 1(d) one observes two dispersive light bands and a portion of heavy band close to the Fermi level, whereas the other part of the heavy band, with bottom about 62 meV below E_F , can be seen in Fig. 1(c).

To understand the originality of the 2DES in CaTiO_3 , it is instructive to compare its electronic structure with that found in SrTiO_3 . Figs. 1(e, f) show, respectively, the Fermi surface and $E - k$ map obtained at the Al-capped $\text{SrTiO}_3(001)$ surface – a protocol recently developed by us to create highly homogeneous 2DES on several oxides [19]. We thus identify three bands, two light and one heavy, in the $E - k$ maps of both materials. In SrTiO_3 , the two light bands have d_{xy} character, while the heavy band has d_{yz} (d_{xz}) character along k_x (k_y) [10, 11]. For

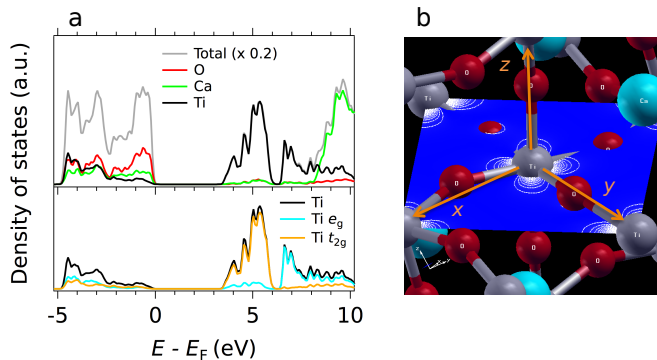


FIG. 2. (a) Top: Total, Ti-, Ca- and O-projected densities of states of bulk CaTiO_3 obtained from HSE calculations. Bottom: Decompositions into Ti e_g ($d_{z^2} + d_{x^2-y^2}$) and Ti t_{2g} ($d_{xy} + d_{yz} + d_{xz}$) components shows that the conduction band minimum of CaTiO_3 is mainly formed of t_{2g} orbitals. (b) Cut into the pseudo- TiO_2 plane (blue plane) of the charge density plot (white contours) for the lower energy state of the conduction band in CaTiO_3 . Ca, Ti, and O atoms are represented by cyan, grey and red spheres, respectively. Orange arrows show the (x, y, z) axes of the pseudo-cubic unit cell.

CaTiO_3 , as will be fully justified by our DFT calculations below, we also identify the subbands as states of the t_{2g} manifold. The two light bands correspond to d_{xy} bands forming circular Fermi surface sheets (see the [Supplementary Material](#) for additional data close to Γ_{005} and Γ_{115} , as well as photon energy dependence of ARPES data in CaTiO_3 , to confirm their orbital and 2D characters). However, the dispersion of the heavy band is clearly different in SrTiO_3 and CaTiO_3 . The rotation of the oxygen octahedra in CaTiO_3 breaks the cubic symmetry of the ideal perovskite lattice (SrTiO_3) and thus can result in the hybridization of orbitals of different azimuthal quantum numbers. The hybridization of the d_{xz} and d_{yz} bands in CaTiO_3 is evident from the star-shaped Fermi surface in Fig. 1(a), which can be understood as resulting from the hybridization of the two elliptic Fermi surface sheets in Fig. 1(e), and is further supported by the non-parabolic dispersion as well as the light polarization dependence of the heavy band in Figs. 1(c, d). In fact, the dispersions of the heavy subbands in CaTiO_3 can be fitted using a minimal one-layer tight-binding model assuming hybridization of the d_{xz} and d_{yz} bands, as shown by the red curves in Figs. 1(a, c, d). Based on such model, Figs. 1(g, h, i) show the momentum-resolved fraction of the orbital character of the hybrid heavy band, demonstrating the hybridization between the d_{xz} and d_{yz} orbitals in CaTiO_3 , and the pure d_{xz} orbital character of the heavy band in SrTiO_3 . Details on the used tight-binding model are provided in the [Supplementary Material](#).

From Fig. 1(c, d), the bottoms of the d_{xy} subbands at the surface of CaTiO_3 are located at -158 meV and

-27 meV, while the bottom of the hybrid (d_{xz}, d_{yz}) heavy subband is at -62 meV. Parabolic fits around Γ yield an effective mass of approximately $m_{d_{xy}} = 1.1 m_e$ for the d_{xy} bands, and $m_{d_{xz}, yz}(\Gamma) = 2.7 m_e$ for the heavy band. Based on the tight-binding model described before, the mass of the heavy band sufficiently away from Γ (close to its Fermi momenta k_F , where orbital hybridization is negligibly small) is $m_{d_{xz}, yz}(k_F) \approx 15 m_e$. The Fermi momenta of the d_{xy} subbands are 0.07 \AA^{-1} and 0.20 \AA^{-1} , and 0.38 \AA^{-1} for the hybrid heavy subband. This gives an electron concentration of $n_{2D} \approx 1.2 \times 10^{14} \text{ cm}^{-2}$, or about 0.17 electrons per a^2 , where a is the pseudo-cubic lattice constant of the orthorhombic lattice.

Numerical calculations.- We carried out DFT calculations to understand how the rotation of the oxygen octahedra surrounding the Ti^{4+} cation, and the concomitant altered bonding angle Ti-O-Ti, affect the orbital order of the crystal field split t_{2g} (d_{xy}, d_{yz}, d_{xz}) and e_g ($d_{z^2}, d_{x^2-y^2}$) orbitals in bulk CaTiO_3 . In fact, as shown by the projected densities of states in Fig. 2(a), top panel, the top of the valence band (set as zero of energy) has mostly oxygen character, while Ti states contribute mainly to the bottom of the conduction band (CB). Moreover, as demonstrated in Fig. 2(a), bottom panel, a decomposition into Ti e_g and t_{2g} components shows that the CB minimum displays predominantly a t_{2g} character, consistent with the octahedral environment of Ti cations. Thus, despite the non-negligible tilt of the TiO_6 octahedra in the bulk CaTiO_3 structure, the contribution of the e_g component to the bottom of CB is small, and it totally vanishes at the CB minimum at Γ . Thus, the 2DES at the (001) surface of CaTiO_3 should be mainly composed of the t_{2g} states, which justifies the choice of tight-binding orbitals used to fit the experimental data in Fig. 1. In fact, as shown in Fig. 2(b), the projection of the lower-energy conduction state into the experimentally studied pseudo- TiO_2 plane shows clearly that the electron wave function in this plane presents the symmetry of t_{2g} orbitals. The [Supplementary Material](#) presents a detailed description of our DFT calculations.

Comparison between various ATiO_3 perovskites.- The 2DES at the surface of CaTiO_3 , presented in this paper, is a new member of the family of ATiO_3 perovskites hosting a 2DES on its surface (SrTiO_3 and BaTiO_3) [10, 19]. The comparison of these 2DES gives insight into the coupling of the electronic structure to different lattice symmetries, as the three oxides show fundamentally different lattice distortions. While SrTiO_3 is (close to) the perfect cubic perovskite structure, the oxygen octahedra are rotated in CaTiO_3 , and in BaTiO_3 the Ti cation moves away from the center of the octahedra resulting in a ferroelectric distortion. These rotations/distortions and the corresponding electronic structure of the 2DES's, based on our ARPES measurements, are schematized in Figs. 3(a, b, c). The ARPES results on the 2DES's are also summarized in

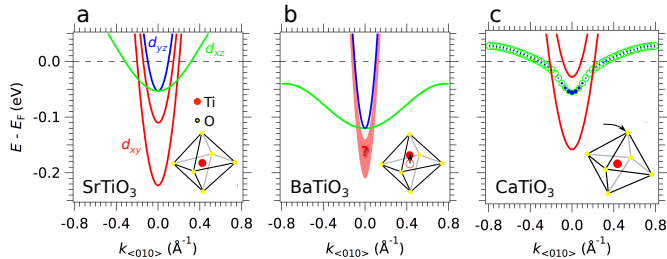


FIG. 3. Oxygen octahedra in $ATiO_3$ ($A=Sr,Ba,Ca$) perovskites and schematic of band dispersion observed in the 2DESs in $SrTiO_3$ (a), $BaTiO_3$ (b) and $CaTiO_3$ (c). The black arrows in (b) and (c) indicate the distortion occurring in $BaTiO_3$ and $CaTiO_3$. The broad red band and the question mark in (b) indicate that the band structure of the d_{xy} band was not resolved well by ARPES in $BaTiO_3$. The colors of the bands correspond to different orbital characters. The size of the blue filled and green empty circles in (c) represents the fraction of the d_{xz} (green) and the d_{yz} (blue) in the band dispersion.

Table I. The differences in the electron structure will be discussed in the next paragraphs.

The effective mass of the d_{xy} subbands is larger by a factor of 1.6 in $CaTiO_3$ compared to $SrTiO_3$, due to the rotation-induced decrease in the Ti d bandwidth [27]. This reduced bandwidth or respectively, increased density of states was related to a more robust ferromagnetism at the $LaAlO_3/CaTiO_3$ interface compared to the $LaAlO_3/SrTiO_3$ interface, although the driving force for the magnetic order are the d_{xz} and d_{yz} , not the d_{xy} , orbitals [23]. Due to the orbital hybridization of the d_{xz} and d_{yz} bands, $m_{d_{xz},yz}^*$ is about five times smaller close to Γ than far away from Γ (near E_F) in $CaTiO_3$. These insights are also of relevance for $SrTiO_3$ -based heterostructures, as rotations of octahedra can occur at interfaces [27–29].

While the electron densities are rather similar in $CaTiO_3$ and $SrTiO_3$ (factor of 1.2), n_{2D} in $BaTiO_3$ is at least twice as large compared to the other oxides. The ferroelectric polarization in single domain $BaTiO_3/SrTiO_3$ thin films is in the upward direction, *i.e.* towards the surface [30]. The resulting electric field will influence the confining field of the 2DES and thus, the electron density can be altered. Hence, in principle, n_{2D} can be controlled by the polarization in the thin film which can be manipulated by choosing different substrates [30] or by applying strain gradients [31].

The orbital order in 2DESs is mainly determined by the effective mass along the confinement direction m_z^* [10]. As shown previously, the orbital mixing in $CaTiO_3$ influences $m_{d_{xz},yz}^*$ in the surface plane, and will also influence m_z^* for this band. Thus, the combined effects of hybridization and electron confinement determine the orbital order. Consequently, as seen in

Fig. 3 and summarized in table I, the hybridized band in $CaTiO_3$ is *in between* two d_{xy} subbands, in contrast to the $d_{xy} - d_{xz} - d_{yz}$ energy order in $SrTiO_3$ [10, 19].

The orbital order in the 2DES at the $LaAlO_3/SrTiO_3$ interface is essential to understand its properties. Many of the unusual phenomena at this interface are related to the Lifshitz transition occurring at electron densities at which the heavy bands d_{xz}/d_{yz} start to be populated [32–34]. In contrast, other phenomena are only observed in pure d_{xy} systems, *e.g.* the Quantum Hall Effect [35]. In $SrTiO_3$ -based interfaces the control of the orbital order and occupancy is based on adjusting the electron density and the spatial extension as well as depth of the quantum well confining the electrons, depending for example on the composition of the oxide heterostructure [35]. Another way is to choose different surface or interface orientations in $SrTiO_3$ [13, 36]. The present study demonstrates another possibility by choosing different A-site cations in the perovskite lattice. New insights in the properties at the interfaces of complex oxides could be gained by studying Lifshitz transition in 2DESs in $CaTiO_3$ and $BaTiO_3$.

Conclusions.- We studied the coupling between the lattice structure and the electronic structure of 2DES at the surface of three different insulating perovskites $ATiO_3$. Our reference system is the 2DES in cubic

TABLE I. Relationships between crystal structure and electronic properties of the 2DES at the surface of $CaTiO_3$, $SrTiO_3$ and $BaTiO_3$. The Goldschmidt’s tolerance factor and the lattice symmetry are given in the first two rows. The effective masses m^* (in units of the free electron mass m_e) of the d_{xy} and d_{xz},d_{yz} bands are given in the next two rows. The subsequent four rows give the bottom energies of the $E_{t_{2g}}$ bands together with the energy difference between the two d_{xy} subbands, $\Delta E_{d_{xy}}$. The last row gives the electron density n_{2D} of the 2DES. All data correspond to the maximal electron density observed for each of the 2DES.

	$CaTiO_3$	$SrTiO_3$ [19]	$BaTiO_3$ [19]
Tolerance	0.97	1.01	1.08
Phase at RT	orthorhombic	cubic	tetragonal
$m_{d_{xy}}^*/m_e$	1.1	0.7	0.3 ± 0.2^a
$m_{d_{xz}/yz}^*/m_e$	2.7 at Γ	7 ± 1	10 ± 2
$E_{d_{xy}}^{(1)}$ (meV)	158	223	200 ± 60^a
$E_{d_{xy}}^{(2)}$ (meV)	27	110	–
$\Delta E_{d_{xy}}$ (meV)	131	113	–
$E_{d_{xz}/yz}$ (meV)	62	50	135 ± 10
Orbital order	$xy, (xz/yz), xy$	$xy, xy, xz/yz$	$xy, xz/yz$
n_{2D} (10^{14}cm^{-2})	1.2	1.4	2.8 ± 0.4

^a The dispersion of the light d_{xy} band in $BaTiO_3$ has not been resolved well by ARPES. The light electron mass $m_{d_{xy}}^*$ is estimated from the band bottom and Fermi momenta of the d_{xz} or d_{yz} band along the “light” direction (x for d_{xz} , y for d_{yz}). The estimated band bottom $E_{d_{xy}}^{(1)}$ is based on the spectral weight distribution of the d_{xy} band in [19].

SrTiO₃ which has been intensively studied at its bare surface as well as at the LaAlO₃/SrTiO₃ interface. The orthorhombic distortions in CaTiO₃ result in a hybridization of the d_{xz} and d_{yz} orbitals. The ferroelectric distortions in BaTiO₃ result in a macroscopic polarization which influences the electron density of the 2DES. Moreover, the distortions change band width as well as the orbital order of the t_{2g} manifold in the 2DES. Both band width and orbital order influence the macroscopic, *e.g.* magnetic and transport, properties of the 2DESs [23, 33]. Our results motivate the study of interfaces beyond SrTiO₃ as so far the question of whether the properties of the LaAlO₃/SrTiO₃ interface can be generalized to 2DES in other perovskite oxides remains largely unanswered.

We thank Cédric Baumier for help during ARPES experiments, and Marcelo Rozenberg for discussions. This work was supported by public grants from the French National Research Agency (ANR), project LACUNES No ANR-13-BS04-0006-01, the “Laboratoire d’Excellence Physique Atomes Lumière Matière” (LabEx PALM projects ELECTROX and 2DEGS2USE) overseen by the ANR as part of the “Investissements d’Avenir” program (reference: ANR-10-LABX-0039), and the CNRS-CONICET 2015-2016 collaborative project AMODOX (project number: 254274). T. C. R. thanks funding from the RTRA–Triangle de la Physique (project PEGASOS). R. W. acknowledges support from CONICET (grant No. PIP 114-201101-00376), and ANPCyT (grant No. PICT-2012-0609). M. G. and A.F.S.-S. acknowledge the support received from the Institut Universitaire de France.

SUPPLEMENTARY MATERIAL

Surface preparation

Single crystals of CaTiO₃ of $5 \times 5 \times 0.5$ mm³ were provided by SurfaceNet GmbH. To clean the polished surface, the crystal was annealed in ultra high vacuum at a temperature of about 550-600°C, as at this temperature most carbon-based compound desorb from the surface of the closely related perovskite SrTiO₃ [37]. The resulting low energy electron diffraction (LEED) image in Fig. 4 shows an unreconstructed surface. Alternatively, single crystals were fractured at low temperatures $T = 7$ –20 K in ultra high vacuum. The fractured surfaces were not characterized by electron diffraction. However, the periodicity of the electronic structure from ARPES measurements demonstrates the surface crystallinity and the absence of surface reconstructions.

Creation of oxygen vacancies

As in previous works, the 2DES is formed by the creation of oxygen vacancies due to desorption induced by UV irradiation [38] or due a redox reaction with Al [19]. Fig. 5(a) shows a comparison between the stoichiometric surface (red curve) and the surface reduced by the synchrotron beam (blue curve) after the oxygen depletion reached a saturation value at the given temperature and photon flux. Oxygen vacancies produce an electron transfer from oxygen to Ti, as evidenced by the shoulder of the Ti 3*p* peak corresponding to Ti³⁺ cations, and the in-gap state as well as the 2DES formed close to the Fermi level E_F . As in other reduced oxide surfaces, the in-gap state corresponds to electrons localized at Ti cations close to the vacancy whereas the 2DES represents itinerant electrons [18, 39]. This dual character of excess electrons and the interplay between the two is essential to understand the magnetic properties of SrTiO₃ based interfaces and surfaces [40].

To roughly estimate the concentration of oxygen vacancies at the surface, the Ti 3*p* peak of the blue curve in Fig. 5(a) is fitted by two Voigt peaks, corresponding to the Ti⁴⁺ and Ti³⁺ contributions, and a Shirley background. The fraction of the area of the Ti³⁺ Voigt peak is about 36% compared to the total area of the Ti 3*p* peak. Assuming that an oxygen vacancy results in an transfer of two electrons to Ti, the vacancy concentration is about $x = 6\%$ in CaTiO_{3(1-x)}. Note that this value corresponds to the weighted average over the probing depth defined by inelastic mean free path of the photoelectrons in the solid. The concentration of oxygen vacancies varies depending on photon flux, exposure time and temperature. The given value was obtained at a surface in which the effect of oxygen desorption saturated under the given experimental conditions.

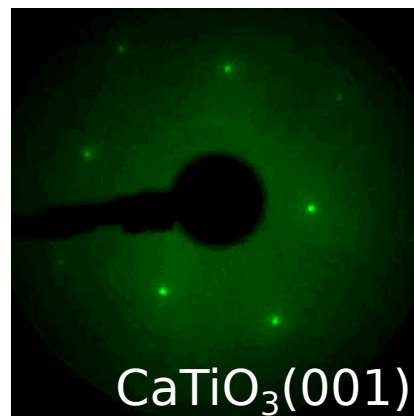


FIG. 4. LEED image of a polished CaTiO₃(001) surface after annealing at approximately $T = 550$ – 600°C in UHV. The kinetic energy of the incident electrons was set to 81 eV.

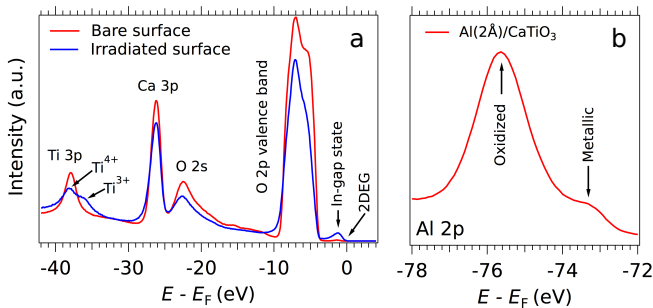


FIG. 5. (a) Angle-integrated spectra of a fractured $\text{CaTiO}_3(001)$ surface measured at a photon energy of $h\nu = 100$ eV showing the partial density of states for binding energies between -42 eV and 2 eV. The red curve was measured right after the first exposure to light whereas the blue one was measured about an hour later. The creation of oxygen vacancies is evidenced by the Ti^{3+} shoulder of the Ti $2p$ peak and the presence of the in-gap state as well as the 2DES. (b) Aluminium $2p$ peak measured at $h\nu = 100$ eV after depositing 2 \AA of aluminium on a clean and polished $\text{CaTiO}_3(001)$ surface. The part of the peak corresponding to oxidized Al demonstrates the occurrence of a redox reaction at the interface of Al and oxide.

The position of the Ti^{4+} peak fitted by a Voigt shape shifts by 230 meV in binding energy between the blue and red curve in Fig. 5(a). This value corresponds to the minimal band bending at the oxygen-deficient surface of CaTiO_3 shown in Fig. 5(a), as it is again a weighted average over the probing depth and a small band bending might already be present at the first measurement (red curve).

Alternatively to the synchrotron irradiation, oxygen vacancies are created by the deposition of 2 \AA of aluminium on the clean and polished surface of CaTiO_3 at temperatures of about $T = 50 - 100^\circ\text{C}$. Details on the Al deposition are described elsewhere [19]. As shown in Fig. 5(b), a large part of the deposited aluminium is oxidized as evidenced by the peak at about -75.6 eV, and only a small part is still metallic (peak at about -73 eV).

DFT: Computational method and settings

Most of the calculations were performed within the Density Functional Theory (DFT), implemented in VASP (Vienna ab initio simulation package) [41, 42]. Gradient-corrected GGA (PW91) [43], GGA+U [44] ($U = 5.0$ eV, $J = 0.64$ eV), and hybrid (HSE06) [45, 46] exchange-correlation functionals were used to give robust grounds for the description of the electronic structure of the bulk. The interaction of valence electrons with ionic cores was described within the projector augmented wave (PAW) method [47, 48], and the Kohn-Sham orbitals were developed on a plane-wave basis set. Standard Cal-

cium and Titanium (including $3p$ electrons in the valence band), and soft oxygen (energy cutoff of 270 eV) pseudopotentials provided with VASP were used [47, 48], enabling a full structural relaxation of all considered systems at the hybrid level. The applicability of soft oxygen pseudopotential was validated on the GGA+U level, with results obtained with both the soft and full (energy cutoff of 400 eV) oxygen pseudopotentials. Table II shows a perfect agreement of the calculated structural (lattice parameters and tilt angles) and electronic (band gap) characteristics of bulk CaTiO_3 obtained with the two types of pseudopotentials.

In CaTiO_3 , the Ca^{2+} cations are too small to fit in a undistorted cubic perovskite which results in a $a^-a^-c^+$ rotation (Glazer notation [49]) of the oxygen octahedra surrounding the Ti^{4+} cation and hence, an altered bonding angle Ti-O-Ti. For the bulk calculations we used such orthorhombic unit cell optimizing its shape and volume until all elements of the stress tensor were smaller than 0.01 eV/\AA^3 . Simultaneously, positions of all atoms were optimized so as to make all forces less than 0.01 eV/\AA . With these settings a $(6 \times 6 \times 4)$ Γ -centered Monkhorst Pack sampling of the bulk Brillouin zone assures a convergence of calculated energy differences to 0.02 eV/CaTiO_3 , and of lattice parameters to less than 0.01 \AA . We have done some calculations using the Wien2k package [50], in order to double check our results. In particular, charge density plot showed in Fig. 2(c) of the main text were done using this code.

DFT: Bulk results for different exchange-correlation functionals

Table II summarizes the results obtained for bulk CaTiO_3 at different levels of approximation. Pure GGA predicts a bulk structure (lattice parameters and tilt angles) in relatively good agreement with the experimental data, but largely underestimates the band gap. While the GGA+U approximation considerably improves the band gap, it does not match closely the experimental result despite the large $U - J$ value used in the calculations. Moreover, GGA+U introduces a non-negligible overestimation of the lattice parameters and tilt angles. By contrast, the hybrid approach produces an excellent agreement between the calculated and experimental results in what concerns both the atomic structure and the electronic characteristics.

Projected densities of states are reported in Fig. 6. Regardless of the level of approximation, GGA, GGA+U or HSE and the type of the oxygen pseudopotential used, the top of the valence band has mostly an oxygen character, while Ti states contribute mainly to the bottom of the conduction band. Decomposition into Ti e_g ($d_{z^2} + d_{x^2-y^2}$) and t_{2g} ($d_{xy} + d_{yz} + d_{zx}$) components, obtained by a rotation of the unit cell to the axes of

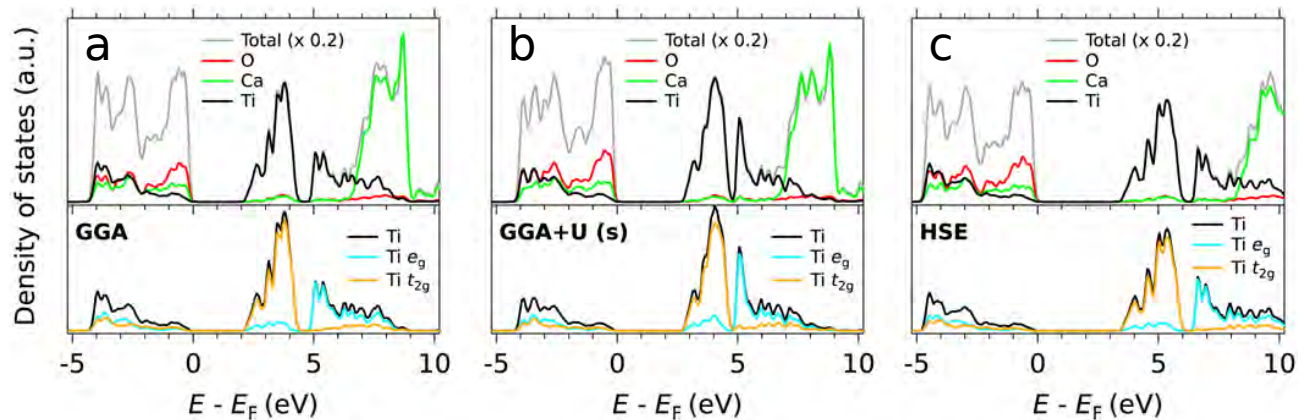


FIG. 6. Total, Ti-, Ca- and O-projected densities of states of bulk CaTiO_3 obtained from standard GGA (a), from GGA+U with soft oxygen pseudopotential (b), and from HSE calculations with soft oxygen pseudopotential (c). The bottom curves of each panel show the decompositions of the Ti-projected density of states into Ti e_g ($d_{z^2} + d_{x^2-y^2}$) and Ti t_{2g} ($d_{xy} + d_{yz} + d_{xz}$) components.

	Exp.	GGA	GGA+U	GGA+U(s)	HSE(s)
a (Å)	5.36	5.40	5.43	5.43	5.36
b (Å)	5.43	5.50	5.55	5.55	5.44
c (Å)	7.62	7.68	7.74	7.73	7.62
ϕ (°)	12	12.1	13.7	13.9	12.3
θ (°)	9	9.2	9.7	9.8	8.8
Gap (eV)	3.50	2.28	2.90	2.90	3.62

TABLE II. Experimental and calculated structural and electronic characteristics of bulk CaTiO_3 : lattice parameters a, b, c (Å), tilt angles θ, ϕ (°), and band gap (eV), obtained from GGA, GGA+U and HSE calculations. (s) denotes results obtained with the soft oxygen pseudopotential.

the conventional cubic unit cell, shows that conduction band minimum displays mainly a t_{2g} character, consistent with the octahedral environment of Ti cations. Despite the non-negligible tilt of the TiO_6 octahedra in the bulk CaTiO_3 structure, the contribution of the e_g component to the bottom of conduction band is small, and it totally vanishes at the CB minimum at Γ . We note that hybrid calculations systematically predict larger bandwidths, as illustrated by the width of the t_{2g} component in the bottom part of conduction band, equal to more than 2.5 eV in HSE and to about 2 eV in GGA+U. The effect of band narrowing is likely linked to the overestimation of the lattice parameters and inter-atomic distances by the GGA+U approximation. We also note that the GGA+U approximation overestimates the tilt of the angles and predicts a larger tilt than either GGA or hybrid approaches, and would thus lead to a larger hybridization of the t_{2g} and e_g states. This feature can also be seen in Fig. 6 where the percentage of the e_g is higher at the bottom of the conduction band as compared to GGA or

hybrid calculations.

Photon energy dependence

The measurement of the photon energy dependence is a way to confirm the confined character of the electronic states, as changing the photon energy corresponds to probing the electronic structure along the confinement direction or respectively, perpendicular to the surface. Based on Heisenberg's principle, confinement in real space results in a large uncertainty of the momentum, *i.e.* non-dispersing bands along the confinement direction in reciprocal space. Previous studies on the 2DES in perovskites demonstrated that d_{xy} orbitals form tubular Fermi surfaces along the confinement direction due to their 2D character [19, 51]. In contrast, the bands of d_{xz} and d_{yz} bands disperse, forming neither purely 2D nor strictly 3D states [19, 51].

Fig. 7 shows that similar dispersions can be observed in the 2DES at the (001) surface of CaTiO_3 . Using linear horizontal (LH) polarization the band of mixed (d_{xz}, d_{yz}) orbital character can be probed close to normal emission (compare to Figs. 1(a, c) in the main text measured at $h\nu = 57$ eV). As displayed by the Fermi surface map in Fig. 7(a), this band disperses along the confinement direction and is thus not strictly 2D. Using linear vertical polarization the light bands shown in Fig. 1(d) of the main text can be measured. As evident from Fig. 7(b,c) these bands are non-dispersing perpendicular to the surface. *Their non-dispersing character confirms the d_{xy} character of these two bands.* Note that the ARPES intensity measured at different photon energies was normalized in Fig. 7 to enhance the visibility of the dispersing bands at different $k_{(001)}$ values.

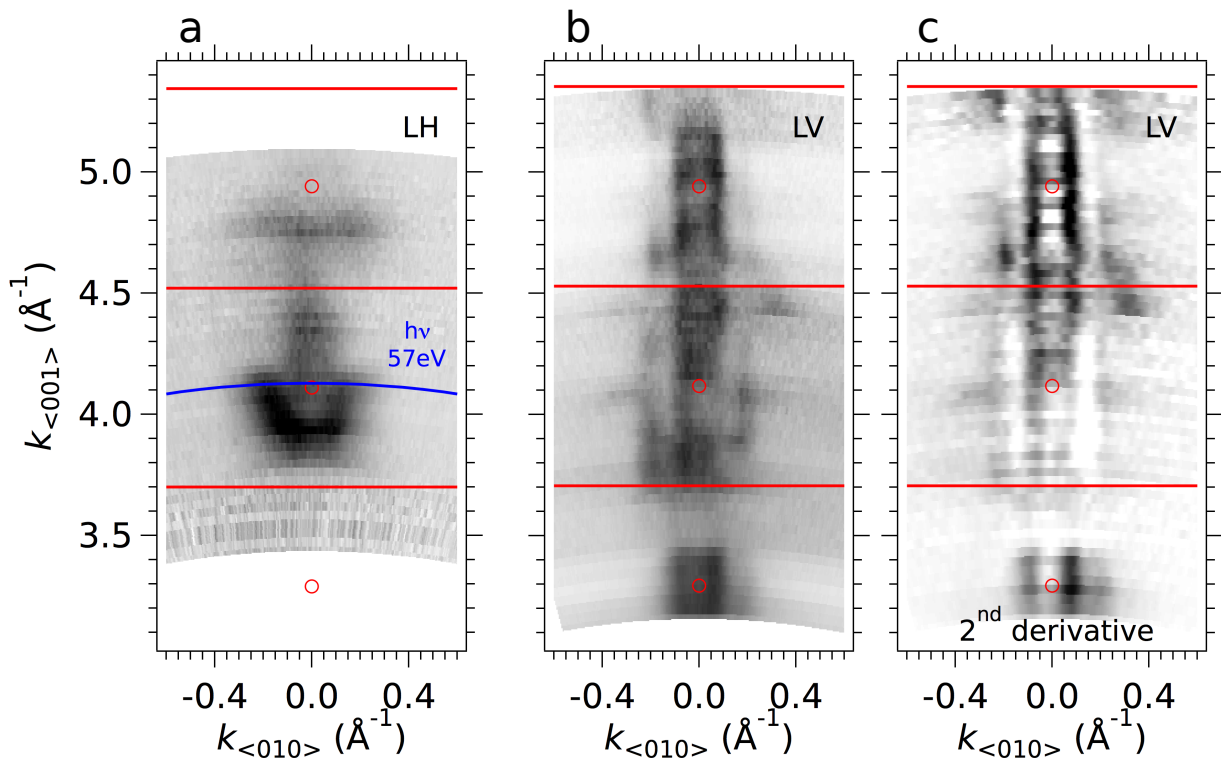


FIG. 7. 2DES at the (001) surface of CaTiO₃. (a) Fermi surface map in the $k_{\langle 001 \rangle} - k_{\langle 010 \rangle}$ plane measured by changing the photon energy between $h\nu = 37$ eV and $h\nu = 90$ eV using linear horizontal polarization. The $\langle 001 \rangle$ direction is the confinement direction perpendicular to the surface. To relate the photon energy $h\nu$ to momentum $k_{\langle 001 \rangle}$ the inner potential was set to $V_0 = 12$ eV. The red lines show the Brillouin zone border of the orthorhombic lattice and the red markers correspond to Γ points of the reciprocal lattice. The blue curve corresponds to the cut in reciprocal space at $h\nu = 57$ eV as shown in the E_k maps in Figs. 1(c, d) of the main text. (b) Fermi surface map with photon energies ranging between $h\nu = 30$ eV and $h\nu = 100$ eV using linear vertical polarization. (c) Same as (b) but based on 2^{nd} derivatives of the $E - k$ maps. All shown maps are averaged intensities over an energy range of at most $E_F \pm 10$ meV.

Complete data set measured close to Γ_{005} and Γ_{115}

The ARPES data in Fig. 8 show the Fermi surface and $E - k$ maps measured close to Γ_{005} and Γ_{115} , as well as their 2^{nd} derivatives. The data close to Γ_{005} was measured at $h\nu = 57$ eV at a fractured (001) surface, the one close to Γ_{115} at $h\nu = 67$ eV at the interface between oxidized Al and CaTiO₃(001). Figs. 8(a, c, i, j) are identical to the Figs. 1(a, b, c, d) of the main text. The more complete data set in Fig. 8 confirms the conclusions in the main text: the presence of a star-shaped and two circular Fermi surface sheets or respectively, the presence of a heavy band of hybrid (d_{yz}, d_{xz}) character and two light d_{xy} bands. The shape of the smallest Fermi sheet formed by the upper light band is not unambiguously circular from the Fermi surfaces presented in Figs. 8(b, c, f, g). However, from Figs. 8(i, j), it is evident that the polarization-dependent selection rules of the upper light band are similar to those of the lower light band, *i.e.* silenced for LH polarization and enhanced for LV polarization, as indeed expected for a band of essen-

tially pure d_{xy} character in the experimental geometry of the data presented here [10, 19]. Together with the non-dispersing character of this band along the confinement direction $\langle 001 \rangle$, as shown in Fig. 7(b,c), this indicates a d_{xy} character for the upper light band. As discussed in Fig. 2(a) of the main text, there might be small contributions of e_g states to the bands forming the 2DES.

Note that the electron density of the 2DES at the Al/CaTiO₃ interface is slightly lower than at the bare surface as evidenced by the smaller Fermi momenta and binding energies of the band bottom of the d_{xy} bands in Figs. 8(g,k) compared to Figs. 8(f,j). The given values of Fermi momenta, binding energies and electron densities in the main text correspond to values at the bare surface. The most probable reason for the difference are the different techniques used to prepared the surface and/or create the 2DES.

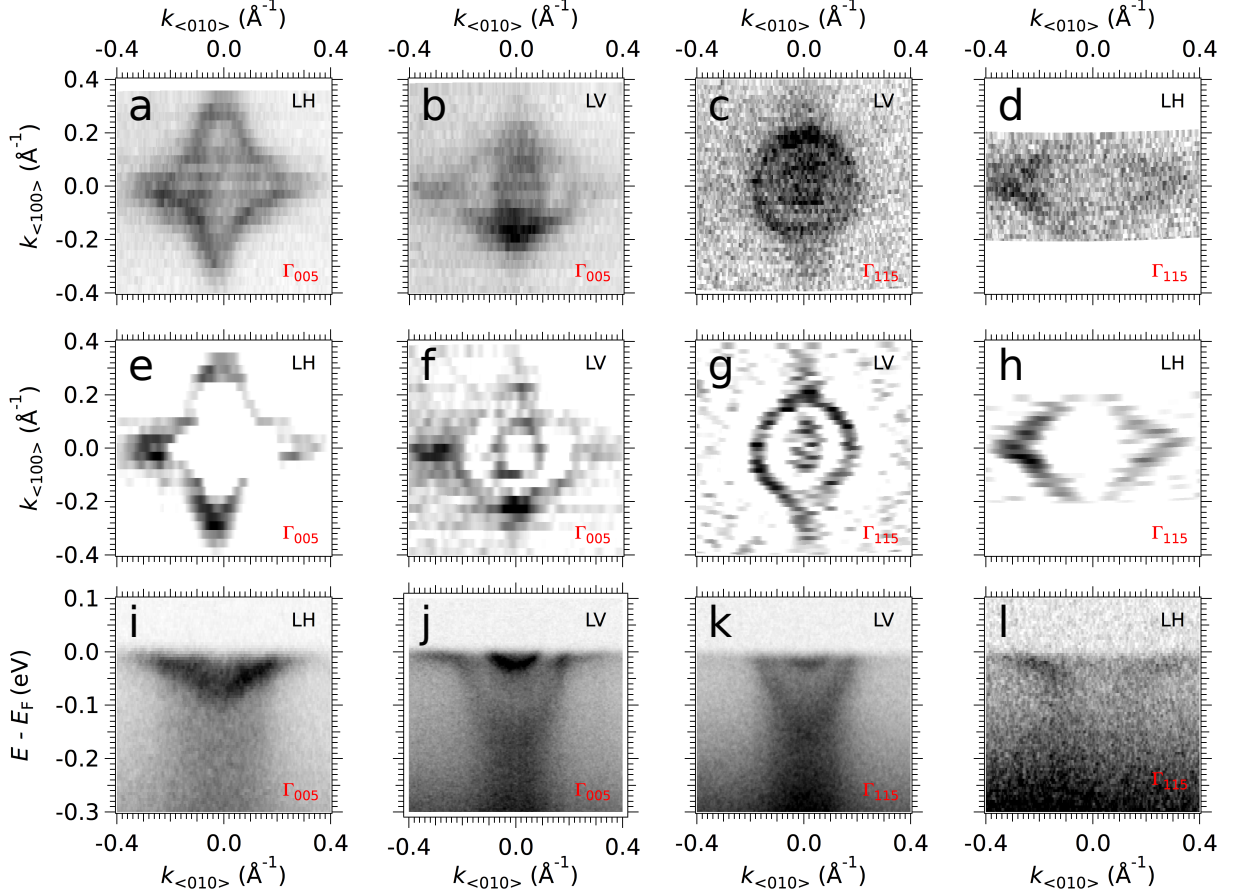


FIG. 8. (a-d) Fermi surface intensity maps measured at the surface of CaTiO₃(001) close to Γ_{005} ($h\nu = 57$ eV) (a,b) and close to Γ_{115} ($h\nu = 67$ eV) (c,d) using LH and LV polarization. The measurements in (a,b) were conducted on a fractured surface of CaTiO₃, whereas in (c,d) the Al(2Å)/CaTiO₃ interface was probed. The maps shown are averaged intensities over an energy range of at most $E_f \pm 10$ meV. (e-h) Same as (a-d) but based on the 2nd derivatives of the $E - k$ maps. (i-l) Corresponding $E - k$ intensity maps through the Γ point.

Tight-binding model

We use a simple tight-binding model to rationalize the orbital hybridization between t_{2g} orbitals in the 2DES of CaTiO₃. We consider the specific case of the d_{yz} and d_{xz} orbitals giving rise to the hybrid heavy band seen in Figs. 1(a,c) of the main text. To reproduce the experimental dispersions and Fermi surfaces it is sufficient to consider the electron hopping between d_{yz} and d_{xz} orbitals on a 2D square lattice. The Hamiltonian H_{XY} of the system in the basis $\{d_I\}$, where $I = (X, Y)$ corresponds to the orbital character (yz, zx) of the two d orbitals, is given by:

$$H_{XY} = \begin{pmatrix} d_X^\dagger \\ d_Y^\dagger \end{pmatrix}^T \begin{pmatrix} \epsilon_X & \epsilon_{XY} \\ \epsilon_{XY}^\dagger & \epsilon_Y \end{pmatrix} \begin{pmatrix} d_X \\ d_Y \end{pmatrix},$$

with

$$\begin{aligned} \epsilon_X &= -2t_{\pi'} \cos(a k_y) - 2t_{\delta'} \cos(a k_x) \\ \epsilon_Y &= -2t_{\pi'} \cos(a k_x) - 2t_{\delta'} \cos(a k_y) \\ \epsilon_{XY} &= -2t_{XY'} (\cos(a k_x) + \cos(a k_y)). \end{aligned}$$

Here, ϵ_X and ϵ_Y describe the intra-layer hopping between identical orbitals, whereas ϵ_{XY} correspond to hopping between different orbital characters. The hopping between nearest neighbors of Ti cations is characterized by the hopping amplitudes $t_{\pi'}$ and $t_{\delta'}$, the hopping between the d_{xz} and d_{yz} orbitals by $t_{XY'}$. The Greek letters in the indices of the hopping amplitudes correspond to the type of chemical bonding (π, δ). The tight-binding fit for the hybrid heavy band in CaTiO₃, shown in Figs. 1(a, c, d) of the main text, is based on $t_{\pi'} = 0.24$ eV, $t_{\delta'} = 0.017$ eV, and $t_{XY'} = 0.010$ eV. The hopping amplitude $t_{\pi'}$ is defined by the effective mass $m_{d_{xy}}^*$ of the d_{xy} band near Γ : $t_{\pi} = \hbar^2 / (2m_{d_{xy}}^* a^2)$, where

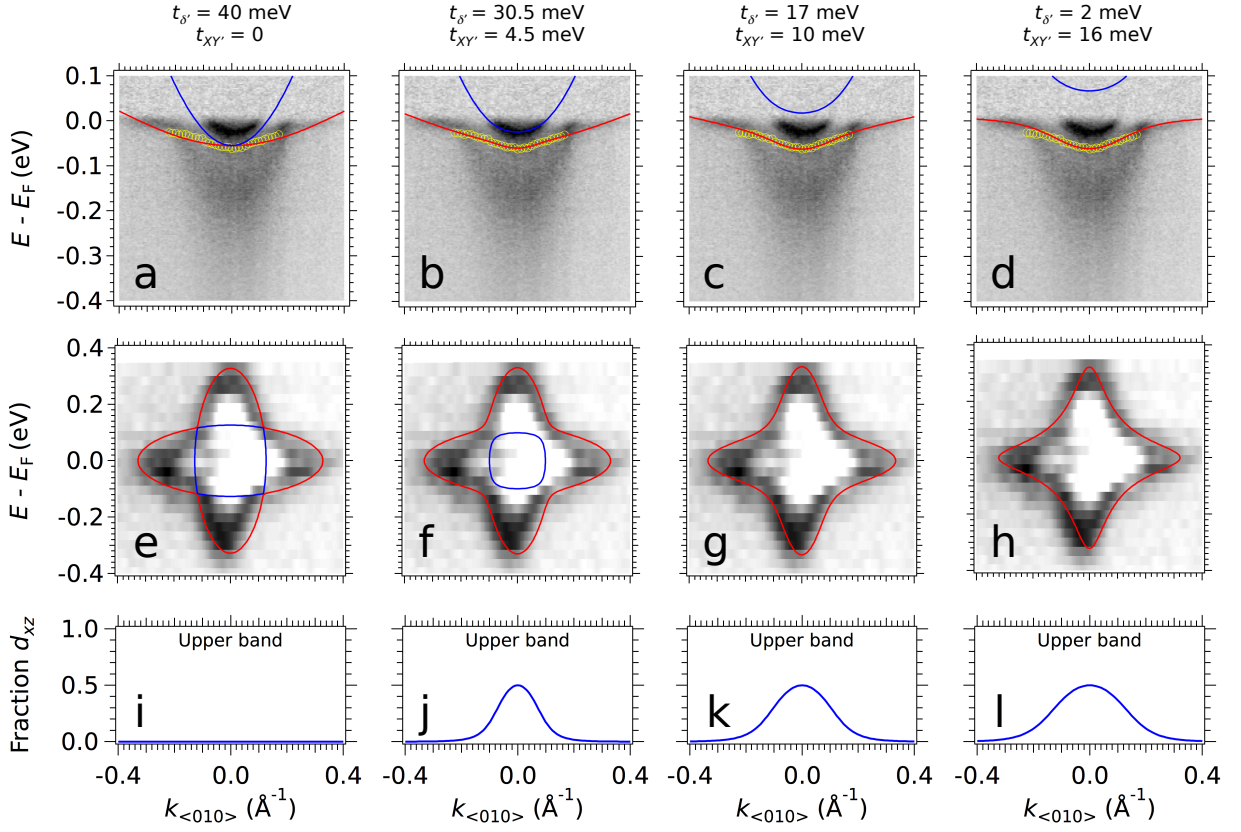


FIG. 9. (a-d) ARPES $E - k$ intensity maps of the 2DES at the surface $\text{CaTiO}_3(001)$ close to Γ_{005} , measured with LV photons at $h\nu = 57$ eV. The yellow markers are the experimental peak positions of the hybridized heavy band measured using LH photons at the same energy –see Fig. 1(c) of the main text. The red and blue curves are tight-binding models of the d_{xz}/d_{yz} doublet for different hopping amplitudes between identical orbitals along δ bonds ($t_{\delta'}$) and different hybridization energies between d_{xz} and d_{yz} orbitals ($t_{XY'}$), as specified on top of each panel. In all cases, the parameters are set to provide the best fit to the heavy hybridized band for a given $t_{XY'}$. (e-h) Fermi surface of the 2DES at the surface $\text{CaTiO}_3(001)$ close to Γ_{005} , measured with LH photons at $h\nu = 57$ eV, to enhance the Fermi surface formed by the hybridized heavy band –as discussed in Fig. 1 of the main text. The red and blue curves are the tight-binding Fermi surfaces from the corresponding models in panels (a-d). (i-l) Fraction of d_{xz} orbital character along $k_{<010>}$ (*i.e.* k_y) for the upper band in the hybridized d_{xz}/d_{yz} doublet.

$a \approx 3.82 \text{ \AA}$ the lattice constant of the quasi-square lattice. $t_{\delta'}$ and $t_{XY'}$ are adjusted to fit simultaneously the experimental band dispersion and Fermi surface of the hybrid heavy band. In the case of SrTiO_3 , $t_{\pi'}$ is calculated based on $m_{d_{xy}}^* = 0.7m_e$ in table I of the main text (m_e is the free electron mass), and $t_{\delta'}$ based on $m_{d_{xz}/yz}^* \approx 7m_e$.

Note that the tight-binding parameters to fit the electronic structure of the 2DES in CaTiO_3 are not unambiguous –the main reason being the simplicity of the model. Fig. 9 shows fits to the hybrid heavy band and Fermi surface for different sets of parameters, from the case of no hybridization between the d_{xz} and d_{yz} orbitals, Figs. 9(a, e, i), to the case of a hybridization energy of 16 meV, Figs. 9(d, h, l). Comparing Figs. 9(a, e) with (b, f), (c, g) or (d, h), it is clear that a certain hybridization between the d_{yz} and d_{xz} orbitals is necessary to reproduce the dispersion and Fermi surface of the hybrid

heavy band –the fits becoming better as the hybridization energy approaches 16 meV. However, considering only the tight-binding model does not clarify the origin of the upper light band forming the inner quasi-circular Fermi sheet. In one case, as shown in Figs. 9(b, f), such light band would correspond to the upper band of the pair formed by the hybridized d_{xz} and d_{yz} bands. In the other case, as shown in Figs. 9(c, d, g, h), the upper band of the hybridized doublet would be unoccupied, as the splitting is larger due to a larger hybridization energy, and the experimental upper light band would be the second quantum-well state of the d_{xy} band. As stated in the main text, and discussed previously in this Annex, we assigned d_{xy} character to the upper light band due to both its non-dispersing character along the surface normal, as shown in Figs. 7(b,c), and its polarization-dependent selection rules, Figs. 8(i, j), which are essentially the same as those of the lower light band.

-
- * Present address: Laboratory for Photovoltaics, Physics and Material Science Research Unit, University of Luxembourg, L-4422 Belvaux, Luxembourg
 † andres.santander@csnsm.in2p3.fr
- [1] E. Dagotto and Y. Tokura, *MRS Bull.* **33**, 1037 (2008).
 - [2] P. Zubko, S. Gariglio, M. Gabay, P. Ghosez, and J.-M. Triscone, *Annu. Rev. Condens. Matter Phys.* **2**, 141 (2011).
 - [3] V. M. Goldschmidt, *Naturwissenschaften* **14**, 477 (1926).
 - [4] M. L. Medarde, *J. Phys. Condens. Matter* **9**, 1679 (1997).
 - [5] T. Kimura, S. Ishihara, H. Shintani, T. Arima, K. Takahashi, K. Ishizaka, and Y. Tokura, *Phys. Rev. B* **68**, 060403 (2003).
 - [6] A. Ohtomo and H. Y. Hwang, *Nature* **427**, 423 (2004).
 - [7] D. A. Dikin, M. Mehta, C. W. Bark, C. M. Folkman, C. B. Eom, and V. Chandrasekhar, *Phys. Rev. Lett.* **107**, 056802 (2011).
 - [8] L. Li, C. Richter, J. Mannhart, and R. C. Ashoori, *Nat. Phys.* **7**, 762 (2011).
 - [9] G. Cheng, M. Tomczyk, S. Lu, J. P. Veazey, M. Huang, P. Irvin, S. Ryu, H. Lee, C.-B. Eom, C. S. Hellberg, and J. Levy, *Nature* **521**, 196 (2015).
 - [10] A. F. Santander-Syro, O. Copie, T. Kondo, F. Fortuna, S. Pailhès, R. Weht, X. G. Qiu, F. Bertran, A. Nicolaou, A. Taleb-Ibrahimi, P. Le Fèvre, G. Herranz, M. Bibes, N. Reyren, Y. Apertet, P. Lecoeur, A. Barthélémy, and M. J. Rozenberg, *Nature* **469**, 189 (2011).
 - [11] W. Meevasana, P. D. C. King, R. H. He, S.-K. Mo, M. Hashimoto, A. Tamai, P. Songsiririttigul, F. Baumberger, and Z.-X. Shen, *Nat. Mater.* **10**, 114 (2011).
 - [12] Z. Wang, Z. Zhong, X. Hao, S. Gerhold, B. Stoger, M. Schmid, J. Sanchez-Barriga, A. Varykhalov, C. Franchini, K. Held, and U. Diebold, *Proc. Natl. Acad. Sci.* **111**, 3933 (2014), arXiv:arXiv:1309.7042v1.
 - [13] T. C. Rödel, C. Bareille, F. Fortuna, C. Baumier, F. Bertran, P. Le Fèvre, M. Gabay, O. H. Cubelos, M. J. Rozenberg, T. Maroutian, P. Lecoeur, and A. F. Santander-Syro, *Phys. Rev. Appl.* **1**, 051002 (2014).
 - [14] S. McKeown Walker, A. de la Torre, F. Y. Bruno, A. Tamai, T. K. Kim, M. Hoesch, M. Shi, M. S. Bahramy, P. D. C. King, and F. Baumberger, *Phys. Rev. Lett.* **113**, 177601 (2014).
 - [15] P. D. C. King, R. H. He, T. Eknapakul, P. Buaphet, S.-K. Mo, Y. Kaneko, S. Harashima, Y. Hikita, M. S. Bahramy, C. Bell, Z. Hussain, Y. Tokura, Z.-X. Shen, H. Y. Hwang, F. Baumberger, and W. Meevasana, *Phys. Rev. Lett.* **108**, 117602 (2012).
 - [16] A. F. Santander-Syro, C. Bareille, F. Fortuna, O. Copie, M. Gabay, F. Bertran, A. Taleb-Ibrahimi, P. Le Fèvre, G. Herranz, N. Reyren, M. Bibes, A. Barthélémy, P. Lecoeur, J. Guevara, and M. J. Rozenberg, *Phys. Rev. B* **86**, 121107(R) (2012).
 - [17] C. Bareille, F. Fortuna, T. C. Rödel, F. Bertran, M. Gabay, O. H. Cubelos, A. Taleb-Ibrahimi, P. Le Fèvre, M. Bibes, A. Barthélémy, T. Maroutian, P. Lecoeur, M. J. Rozenberg, and A. F. Santander-Syro, *Sci. Rep.* **4**, 3586 (2014).
 - [18] T. C. Rödel, F. Fortuna, F. Bertran, M. Gabay, M. J. Rozenberg, a. F. Santander-Syro, and P. L. Fèvre, *Phys. Rev. B* **92**, 041106(R) (2015), arXiv:1507.03916.
 - [19] T. C. Rödel, F. Fortuna, S. Sengupta, E. Frantzeskakis, P. Le Fèvre, F. Bertran, B. Mercey, S. Matzen, G. Agnus, T. Maroutian, P. Lecoeur, and A. F. Santander-Syro, *Adv. Mater.* **28**, 1976 (2016).
 - [20] C. Chen, J. Avila, E. Frantzeskakis, A. Levy, and M. C. Asensio, *Nat. Commun.* **6**, 8585 (2015).
 - [21] Z. Wang, S. McKeown Walker, A. Tamai, Z. Ristic, F. Y. Bruno, A. de la Torre, S. Riccò, N. Plumb, M. Shi, P. Hlawenka, J. Sanchez-Barriga, A. Varykhalov, T. K. Kim, M. Hoesch, P. D. C. King, W. Meevasana, U. Diebold, J. Mesot, M. Radović, and F. Baumberger, *Nat. Mater.* , doi:10.1038/nmat4623 (2016), arXiv:arXiv:1506.01191v1.
 - [22] J. M. Rondinelli, S. J. May, and J. W. Freeland, *MRS Bull.* **37**, 261 (2012).
 - [23] N. Ganguli and P. J. Kelly, *Phys. Rev. Lett.* **113**, 127201 (2014).
 - [24] Z. Liao, N. Gauquelin, R. J. Green, S. Macke, J. Gonnissen, S. Thomas, Z. Zhong, L. Li, L. Si, S. Van Aert, P. Hansmann, K. Held, J. Xia, J. Verbeeck, G. Van Tendeloo, G. A. Sawatzky, G. Koster, M. Huijben, and G. Rijnders, (2017).
 - [25] K. S. Knight, *J. Alloys Compd.* **509**, 6337 (2011).
 - [26] K. Ueda, H. Yanagi, H. Hosono, and H. Kawazoe, *J. Phys.: Condensed Matter* **3535** (1999).
 - [27] Z. Zhong and P. J. Kelly, *Europhys. Lett.* **84**, 27001 (2008).
 - [28] C. L. Jia, S. B. Mi, M. Faley, U. Poppe, J. Schubert, and K. Urban, *Phys. Rev. B* **79**, 081405 (2009).
 - [29] A. Rubano, C. Aruta, U. S. D. Uccio, F. M. Granozio, L. Marrucci, T. Günter, T. Fink, M. Fiebig, and D. Paparo, *Phys. Rev. B* **88**, 245434 (2013).
 - [30] J. Chen, Y. Luo, X. Ou, G. Yuan, Y. Wang, Y. Yang, J. Yin, and Z. Liu, *J. Appl. Phys.* **113**, 204105 (2013).
 - [31] H. Lu, C.-W. Bark, D. Esque de los Ojos, J. Alcalá, C. B. Eom, G. Catalan, and A. Gruverman, *Science* (80-). **336**, 59 (2012).
 - [32] A. Joshua, S. Pecker, J. Ruhman, E. Altman, and S. Ilani, *Nat. Commun.* **3**, 1129 (2012).
 - [33] A. Joshua, J. Ruhman, S. Pecker, E. Altman, and S. Ilani, *Proc. Natl. Acad. Sci.* **110**, 9633 (2013).
 - [34] H. Liang, L. Cheng, L. Wei, Z. Luo, G. Yu, C. Zeng, and Z. Zhang, *Phys. Rev. B* **92**, 075309 (2015).
 - [35] F. Trier, G. E. D. K. Prawiroatmodjo, Z. Zhong, D. V. Christensen, M. von Soosten, A. Bhowmik, J. M. Garcia Lastra, Y. Chen, T. S. Jespersen, and N. Pryds, arXiv Prepr. , 1603.02850v1 (2016), arXiv:arXiv:1603.02850v1.
 - [36] G. Herranz, G. Singh, N. Bergeal, A. Jouan, J. Lesueur, J. Gázquez, M. Varela, M. Scigaj, N. Dix, F. Sánchez, and J. Fontcuberta, *Nat Commun* **6**, 6028 (2015).
 - [37] M. Kawasaki, A. Ohtomo, and T. Arakane, *Appl. Surf. Sci.* **107**, 102 (1996).
 - [38] S. M. Walker, F. Y. Bruno, Z. Wang, A. de la Torre, S. Riccò, A. Tamai, T. K. Kim, M. Hoesch, M. Shi, M. S. Bahramy, P. D. C. King, and F. Baumberger, *Adv. Mater.* **27**, 3894 (2015).
 - [39] H. O. Jeschke, J. Shen, and R. Valenti, *New J. Phys.* **17**, 023034 (2015), arXiv:arXiv:1407.7060v1.
 - [40] F. Lechermann, H. O. Jeschke, A. J. Kim, S. Backes, and R. Valenti, *Phys. Rev. B* **93**, 121103(R) (2016).
 - [41] G. Kresse and J. Furthmüller, *Phys. Rev. B* **54**, 11169 (1996).
 - [42] G. Kresse and J. Hafner, *Phys. Rev. B* **47**, 558 (1993).
 - [43] J. P. Perdew, J. A. Chevary, S. H. Vosko, K. A. Jackson, M. R. Pederson, D. J. Singh, and C. Fiolhais, *Phys. Rev.*

- B **46**, 6671 (1992).
- [44] S. L. Dudarev, G. A. Botton, S. Y. Savrasov, C. J. Humphreys, and A. P. Sutton, *Phys. Rev. B* **57**, 1505 (1998).
- [45] J. Heyd, G. E. Scuseria, and M. Ernzerhof, *J. Chem. Phys.* **118**, 8207 (2003).
- [46] J. Paier, M. Marsman, K. Hummer, G. Kresse, I. C. Gerber, and J. G. Angyan, *J. Chem. Phys.* **124**, 154709 (2006).
- [47] P. E. Blöchl, *Phys. Rev. B* **50**, 17953 (1994).
- [48] G. Kresse and J. Joubert, *Phys. Rev. B* **59**, 1758 (1999).
- [49] A. M. Glazer, *Acta Crystallogr.* **B28**, 3384 (1972).
- [50] P. Blaha, K. Schwarz, G. K. H. Madsen, D. Kvasnicka, and J. Luitz, *WIEN2k, An Augmented Plane Wave and Local Orbitals Program for Calculating Crystal Properties* (Techn. Universität Wien, Austria, 2001).
- [51] N. C. Plumb, M. Salluzzo, E. Razzoli, M. Månsson, M. Falub, J. Krempasky, C. E. Matt, J. Chang, M. Schulte, J. Braun, H. Ebert, J. Minár, B. Delley, K.-J. Zhou, T. Schmitt, M. Shi, J. Mesot, L. Patthey, and M. Radović, *Phys. Rev. Lett.* **113**, 086801 (2014).